Phase Diagram and Structural Diversity of a Family of Truncated Cubes: Degenerate Close-Packed Structures and Vacancy-Rich States

Anjan P. Gantapara,[1,*] Joost de Graaf,[1] René van Roij,[2] and Marjolein Dijkstra[1,†]

[1]*Soft Condensed Matter, Debye Institute for Nanomaterials Science, Utrecht University, Princetonplein 5, 3584 CC Utrecht, Netherlands*

[2]*Institute for Theoretical Physics, Utrecht University, Leuvenlaan 4, 3584 CE Utrecht, Netherlands*

(Received 1 March 2013; published 1 July 2013)

Using Monte Carlo simulations and free-energy calculations, we determine the phase diagram of a family of truncated hard cubes, where the shape evolves smoothly from a cube via a cuboctahedron to an octahedron. A remarkable diversity in crystal phases and close-packed structures is found, including a fully degenerate crystal structure, several plastic crystals, as well as vacancy-stabilized crystal phases, all depending sensitively on the precise particle shape. Our results illustrate the intricate relation between phase behavior and building-block shape, and can guide future experimental studies on polyhedral-shaped nanoparticles.

DOI: 10.1103/PhysRevLett.111.015501 PACS numbers: 61.46.Df, 64.70.M−, 64.75.Yz, 82.70.Dd

Recent advances in experimental techniques to synthesize polyhedron-shaped particles, such as faceted nanocrystals and colloids [1–14] and the ability to perform self-assembly experiments with these particles [15–22], have attracted the interest of physicists, mathematicians, and computer scientists [23–27]. Additionally, predicting the densest packings of hard polyhedra has intrigued mathematicians since the time of the early Greek philosophers, such as Plato and Archimedes [28,29]. Modern computer platforms have made it possible to perform simulations of these systems, which has resulted not only in an improved understanding of the experimentally observed phenomenology in colloidal suspensions of such particles, but also in improved *Ansätze* for the morphology of their close-packed configurations [24,30–35].

The self-assembly of the basic building blocks at finite pressures may differ substantially from the packings achieved at high (sedimentation and solvent-evaporation) pressures. For instance, liquid-crystal, plastic-crystal, vacancy-rich simple-cubic, and quasicrystalline mesophases are stabilized by entropy alone under non-close-packed conditions of hard anisotropic particle systems [30–34,36,37]. Predicting the phase behavior from the shape of the building blocks alone is therefore a major challenge in materials science and is crucial for the design of new functional materials. It is thus not surprising that numerous studies have been devoted to providing simple guidelines for predicting the self-assembly from the particle shape alone [32–34].

Recently, Henzie *et al.* [15] reported the shape-controlled synthesis of truncated cubes. In their research, the close-packed crystals of these particles were studied using sedimentation experiments and simulations. They created exotic superlattices, and their results also tested several conjectures on the densest packings of hard polyhedra [23,25–27]. However, Henzie *et al.* did not examine the finite-pressure behavior of the system. Mapping the full phase diagram for the system of truncated cubes is thus important, not only from a fundamental perspective but also to guide future experimental self-assembly studies to fabricate new functional materials with these building blocks.

In this Letter, we investigate the equilibrium phase diagram of a family of truncated hard cubes, which interpolates smoothly between cubes and octahedra via cuboctahedra. Our calculations show that the phase diagram exhibits a remarkably rich diversity in crystal structures that depends sensitively on the particle shape. We find distinct changes in phase behavior and crystal structures even for small variations in the level of truncation. This is an unexpected result, since the particle shape varies smoothly from that of a cube to that of an octahedron by truncation. Moreover, we find that the equilibrium concentration of vacancies, which is already unusually high for a simple-cubic phase of cubes [36], increases at a fixed packing fraction ϕ upon increasing the level of truncation. In this Letter, we identify and describe in detail the different phases that we obtained, as well as the nature of the phase transitions between these phases.

The particles that we investigate are completely specified by the level of truncation $s \in [0, 1]$ and the volume of the particle; see Fig. 1(a) and the Supplemental Material [38] for the definition of the truncated cube and additional details. Two Platonic (cube and octahedron) and three Archimedean (truncated cube, cuboctahedron, and truncated octahedron) solids are members of this family.

Using the floppy-box Monte Carlo method [39–42] in combination with a separating-axis-based overlap algorithm [43], we first numerically determined the densest structure and the corresponding packing fraction; see Fig. 1(b). Note that the packing fraction "curve" is continuous but has discontinuities in its first derivative. Cubes

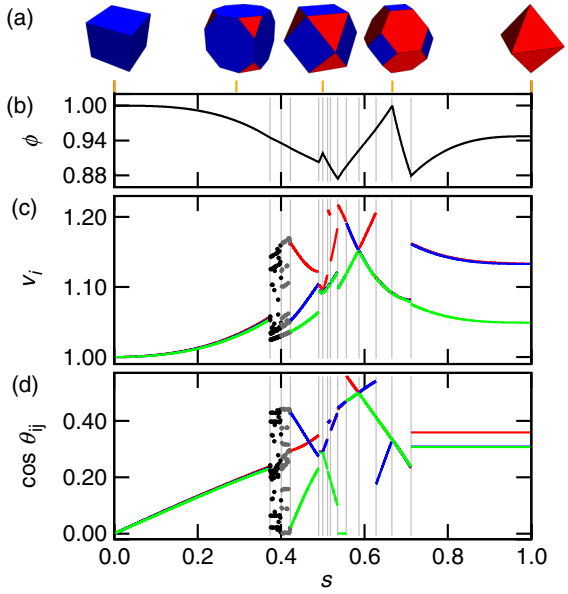

FIG. 1 (color online). (a) Five truncated cubes (Platonic and Archimedean solids only) for levels of truncation s corresponding to the orange lines from left to right: a cube, a truncated cube, a cuboctahedron, a truncated octahedron, and an octahedron. (b) The packing fraction ϕ for the close-packed structures as a function of s. (c) The length v_i ($i = 1, 2, 3$) of the three lattice vectors, indicated in red, green, and blue, that span the unit cell of the densest crystal structure. Not every line is clearly visible, since there is some overlap. Black and gray dots are used in regions with a degeneracy in the crystal structures. (d) The cosine of the angles θ_{ij} ($i < j = 1, 2, 3$) between the three v_i in (b). Gray vertical lines partition the s domain into 14 pieces with a "different" crystal structure, based on the discontinuities of v_i and $\cos\theta_{ij}$.

($s = 0$) and truncated octahedra ($s = 2/3$) are the only shapes that have space-filling close-packed structures in the entire $s \in [0, 1]$ domain. We analyze our results by considering the lengths v_i of and the angles θ_{ij} ($i < j = 1, 2, 3$) between the three lattice vectors that specify the unit cell of the densest crystal structure; these quantities are shown in Figs. 1(c) and 1(d), respectively. Numerical analysis of the discontinuities in the (first derivative of the) ϕ, v_i, and $\cos\theta_{ij}$ curves allows us to partition the $s \in [0, 1]$ domain into 14 distinct regions.

We only briefly discuss the different close-packed structures here, and we refer the interested reader to the Supplemental Material [38] for visual representations and more detailed descriptions. We find (distorted) simple-cubic [(d)sc] phases for $s \in [0.00, 0.374]$. For $s \in (0.374, 0.40]$ and $s \in (0.40, 0.422]$, we observe a large scatter in the lattice vectors, which we expect to approach a continuous spectrum for a larger number of simulations. This corresponds to a degeneracy in the densest crystal structures. The truncated cubes are arranged in a dsc crystal lattice, where the particles form columns that are interlocked in a diagonal way. This prevents lateral motion in the plane normal to the column's direction but allows motion in the direction of the columns for the diagonally interlocked sheets; see Ref. [38] for a visual representation. These structures are referred to as monointerlocking distorted simple-cubic (MI dsc) crystals. For $s \in (0.422, 0.49]$, a dsc crystal phase is found that is interlocking in two directions (BI dsc), while for $s \in (0.49, 0.50)$, a tri-interlocking dsc crystal (TI dsc) is observed. Multiple instances of interlocking prevent motion in the crystal, as also follows from the unicity of the results in these regions in Figs. 1(c) and 1(d). For $s \in [0.50, 0.54]$ and $s \in (0.63, 0.71]$, three different distorted body-centered-tetragonal (dbct) structures are found, and for $s \in (0.54, 0.63]$, there is a regular body-centered-tetragonal (bct) structure. Finally, for $s \in (0.71, 1.00]$, we observe the Minkowski crystal phase. We thus find a remarkable diversity in close-packed structures that depends sensitively on the level of truncation. Below, we investigate the repercussions of the 11 distinct close-packed structures on the behavior at finite pressure.

Using the floppy-box Monte Carlo method results in combination with regular isothermal-isobaric (NPT) simulations and free-energy calculations, we are able to establish the phase diagram for hard truncated cubes, as shown in Fig. 2. For $s < 0.5$, the particles are essentially "cubic" in shape, and we find high-density simple-cubic-like phases. The phase diagram for truncated cubes with shape parameter $s \in [0.00, 0.35]$ displays three stable bulk phases. At very high pressures, we observe a dsc crystal phase similar to the $C1$ phase of Ref. [30]. This phase melts either via a weak first-order or via a second-order phase transition into a vacancy-rich simple-cubic (sc) crystal phase. At even lower pressures, the sc crystal is found to coexist with the fluid phase. For $s \in (0.35, 0.422]$, the phase diagram exhibits four stable phases separated by three two-phase coexistence regions. At sufficiently high pressures, the systems self-assemble into their respective densest-packed structures, which is the dsc ($C1$) structure for $s \in (0.35, 0.374]$ and the MI dsc phase for $s \in (0.374, 0.422]$. Upon lowering the pressure, a first-order transition occurs to the dsc phase with the $C0$-like morphology of Ref. [30]. By further lowering the pressure, the dsc ($C0$) phase melts in all our simulations into a plastic hexagonal close-packed (phcp) crystal structure, before finally melting into a fluid phase. We find a dsc ($C0$)—phcp—liquid triple point at $s \approx 0.374$. For $s \in (0.422, 0.5]$, we observe higher orders of interlocking of the dsc crystal phase at sufficiently high pressures: a BI dsc and a TI dsc crystal, respectively. These phases melt into the phcp phase and subsequently into the isotropic liquid phase upon lowering the pressure, again via first-order phase transitions in both instances. Large lattice vector fluctuations and the degeneracy of the respective crystal structures prohibit free-energy calculations for $s \in [0.35, 0.5]$.

For $s > 0.5$ the shape is "octahedronlike," and we find bct-like structures at close packing. For $s \in [0.5, 0.54]$, the

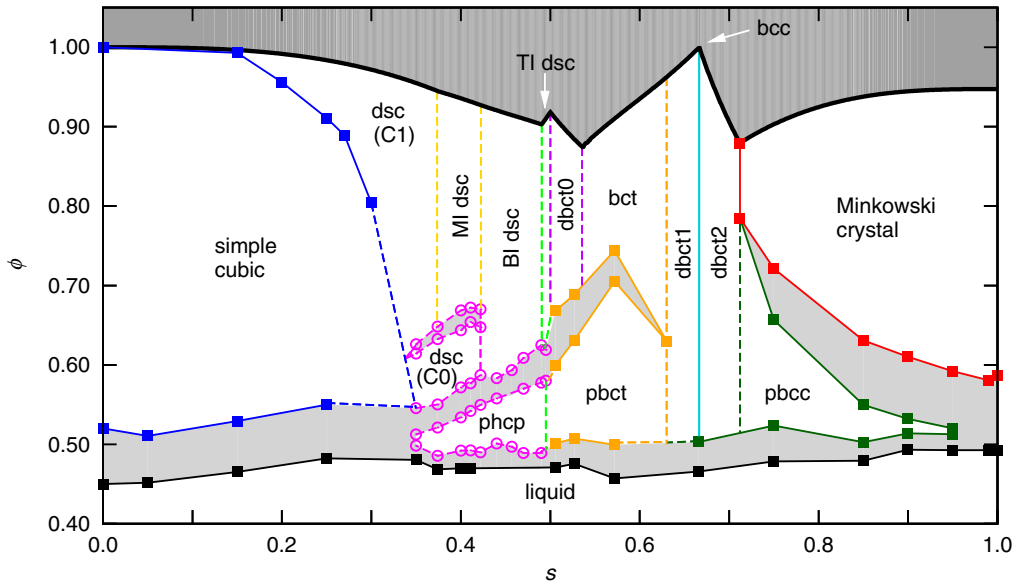

FIG. 2 (color online). Phase diagram for the family of truncated hard cubes in the packing fraction ϕ versus the level of truncation s representation. In the dark-gray area, ϕ exceeds the maximum packing fraction. The light-gray areas indicate the two-phase coexistence regions. The solid square symbols denote the bulk coexistence densities as obtained from free-energy calculations, while the open circles indicate those derived from the equations of state. Coexistence lines that follow from free-energy calculations are represented by solid lines, and those that connect equation-of-state-derived points are given by dashed lines. The numbers that follow the dbct label signify that these dbct phases are distinct. The two dsc phases have different morphologies: one is $C0$-like, and the other is $C1$-like. Finally, the two white arrows in the forbidden region connect the label TI dsc to the small region between the green and purple dashed lines and the label bcc with the turquoise line, respectively.

close-packed dbct phase melts into a plastic bct (pbct) phase upon lowering the pressure via a first-order phase transition. At even lower pressures, we find two-phase coexistence between the pbct and the fluid phase. Interestingly, although the particles in this pbct phase rotate almost freely, their orientational distribution is not isotropic, which gives rise to the pbct rather than a plastic body-centered-cubic (pbcc) phase; see the movie in the Supplemental Material [38]. In the region $s \in (0.54, 0.636]$, we obtain a regular bct phase at high pressures, which undergoes a first-order transition into the pbct phase for intermediate pressures. For $s \in (0.636, 0.712]$, we find two different dbct crystal structures (dbct1 and dbct2 in Fig. 2). The transition between dbct1 and dbct2 is located at $s = 2/3$ (the space-filling truncated octahedron of which all sides are of equal length). Remarkably, this system exhibits a body-centered-cubic (bcc) crystal structure, which exists only for this exact value of the truncation $s = 2/3$. Surprisingly, the close-packed crystal structures in the region $s \in (0.636, 0.712]$ melt directly into a liquid phase via a first-order phase transition upon decreasing the pressure without an intervening plastic-crystal phase. Further increasing the truncation leads to more octahedron-like shapes. In the region $s \in (0.712, 0.95]$, we find a Minkowski crystal [27], which melts into a stable pbcc phase before melting into a fluid. However, for $s \in (0.95, 1.0]$, we find that the intervening pbcc phase becomes metastable with respect to the Minkowski crystal-to-liquid phase transition (see also Ref. [31]), such that at $s = 0.95$, an isotropic liquid—pbcc—Minkowski crystal triple point appears in the phase diagram. Typical configurations of plastic crystals and vacancy-rich simple-cubic phases can be found in the Supplemental Material [38]. The straight lines separating the phase boundaries for $s \in [0.374, 0.712]$ at high packing fractions are a continuation of the subdivision that follows from the distinct crystal structures at close packing. Several simulations close to the boundaries (on either side) are performed, to show that within the numerical accuracy, there is no deviation from the vertical.

Now that we have described the phase diagram, let us return to the vacancy-rich sc phase for $s \in [0.00, 0.374]$. We define the vacancy concentration α as the fraction of unoccupied sites in the sc crystal lattice. To determine the equilibrium vacancy concentration, we calculated the free energy (per particle per $k_B T$) $f(\alpha)$ as a function of α for $s = 0.05$, $s = 0.15$, and $s = 0.25$, at packing fraction $\phi = 0.56$ using the method as described in Ref. [36]. Surprisingly, Fig. 3 shows that the minimum in $f(\alpha)$ shifts to higher α upon increasing the level of truncation s at a fixed packing fraction. This is unlike the behavior observed for parallel cuboids (smooth-edged, parallel-aligned cubes) [37], which exhibit a constant vacancy concentration with increasing roundness at fixed ϕ. The vacancies are delocalized along rows in the crystal lattice, in accordance with

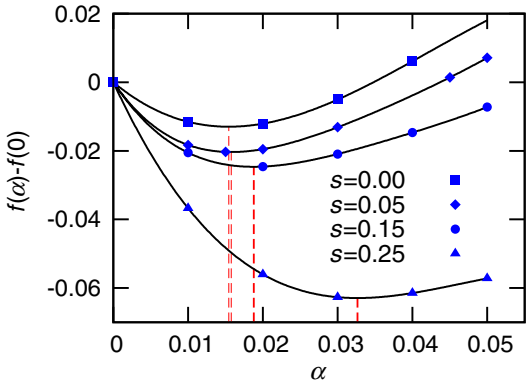

FIG. 3 (color online). Free-energy differences per particle $f = F/(Nk_BT)$ between a system with vacancies $f(\alpha)$ and the one without vacancies $f(0)$ as a function of the fraction of vacancies α for truncations $s = 0$, $s = 0.05$, $s = 0.15$, and $s = 0.25$ at packing fraction $\phi = 0.56$. For $s = 0$, the results are provided by the authors of Ref. [36]. The actual data points are plotted in thick blue symbols; the black line is a polynomial fit to the data. The dashed (red) vertical lines show the location of the minimum in the free energy, i.e., the equilibrium vacancy concentration α.

the results of Ref. [36], since the particles can easily move with respect to each other and fill up the vacated space.

The free energy of a system with vacancy concentration α at a constant packing fraction ϕ and for a given truncation level s is $f(\alpha) = f_{\text{comb}}(\alpha) + f_{\text{def}}(\alpha)$, where $f_{\text{comb}}(\alpha)$ accounts for the combinatorial entropy to place $n \equiv N - N_L$ vacancies at N_L lattice sites, and $f_{\text{def}}(\alpha)$ is the free energy of the crystal system that contains $n = \alpha N_L$ vacancies. In accordance with the observations of Ref. [36], we find that $f_{\text{def}}(\alpha) = f_{\text{def}}(0) + \alpha f_1$ represents the data accurately, suggesting weak interactions between vacancies. Here, $f_{\text{def}}(0)$ is the free energy of a system with no vacancies and $f_1 > 0$ is the free-energy cost to create a single vacancy. We observe that f_1 decreases with s at fixed ϕ, thereby explaining the increase in vacancy concentration with the level of truncation by the reduced free-energy cost to create a vacancy; see the Supplemental Material [38].

It is interesting to compare the present phase diagram to that of hard superballs [30,31] for which the shape interpolates also from cubes to octahedra, but via spheres instead of cuboctahedra. Although there are similarities between the two phase diagrams, such as stable plastic-crystal phases in the center of the phase diagram, there are also striking differences. (i) The stable plastic-crystal regimes are much smaller for polyhedral particles than for superballs. (ii) The phase boundaries of hard superballs change continuously as a function of the shape parameter, whereas the phase boundaries for truncated cubes exhibit sharp transitions. These observations lead to the idea that the more spread-out local curvature of the superballs tends to favor the formation of rotator phases and overall smoother phase behavior, whereas the polyhedral particles with flat faces and sharp edges prefer to align the flat faces to form crystals, which leads to sharp transitions even though s varies smoothly.

Summarizing, we calculated the full phase diagram for a family of truncated cubes, which interpolates smoothly from a cube via a cuboctahedron to an octahedron. The phase diagram shows a remarkable diversity in crystal structures, despite the shape parameter changing smoothly. Of particular interest is the discovery of a fully degenerate crystal phase for certain levels of truncation ($s \approx 0.4$), in which diagonally interlocked sheets of particles can move with respect to each other in *only* one direction. In addition, the latter system is remarkable since it exhibits a fluid state and three different bulk crystals upon increasing the pressure. Both of these qualities may make similarly shaped nanoparticles suitable for the creation of highly tunable functional materials, for which optical, electrical, and rheological properties vary strongly with the bulk pressure of the system. Finally, we showed that the equilibrium vacancy concentration, which is already unusually high for a system of cubes [36], increases even further by truncation at a given ϕ in contrast to the result for parallel cuboids [37].

Although it is tempting to define general guiding rules for the self-assembly of shape-anisotropic particles, the shape sensitivity revealed by the present study shows that one has to be cautious. After all, this also implies that the effect of experimentally inevitable size and shape polydispersity calls for further developments to analyze the stability of structures, e.g., along the lines of Refs. [44,45]. Our present results provide a solid basis for future studies of anisotropic particle systems and pave the way for a full understanding of the recent experimental studies performed on systems of nanoscopic truncated cubes.

We would like to thank F. Smallenburg and L. Filion for providing data for hard cubes and for useful discussions. M. D. and R. v. R. both acknowledge financial support by a NWO-Vici Grant.

*A. P. Gantapara@uu.nl
†M. Dijkstra1@uu.nl

[1] Y. Sun and Y. Xia, Science **298**, 2176 (2002).
[2] E. Matijevic, Acc. Chem. Res. **14**, 22 (1981).
[3] X. Xia and Y. Xia, Nano Lett. **12**, 6038 (2012).
[4] B. Wiley, T. Herricks, Y. Sun, and Y. Xia, Nano Lett. **4**, 1733 (2004).
[5] Y. Wang, Y. Zheng, C. Z. Huang, and Y. Xia, J. Am. Chem. Soc. **135**, 1941 (2013).
[6] J. Zeng, C. Zhu, J. Tao, M. Jin, H. Zhang, Z.-Y. Li, Y. Zhu, and Y. Xia, Angew. Chem., Int. Ed. Engl. **51**, 2354 (2012).
[7] A. S. Barnard, X. M. Lin, and L. A. Curtiss, J. Phys. Chem. B **109**, 24 465 (2005).
[8] X. Zhang, C. Dong, J. Zapien, S. Ismathullakhan, Z. Kang, J. Jie, X. Zhang, J. Chang, C.-S. Lee, and S.-T. Lee, Angew. Chem., Int. Ed. Engl. **48**, 9121 (2009).

[9] H.-L. Wu, C.-H. Kuo, and M. H. Huang, Langmuir **26**, 12 307 (2010).
[10] W. H. Evers, B. Goris, S. Bals, M. Casavola, J. de Graaf, R. v. Roij, M. Dijkstra, and D. Vanmaekelbergh, Nano Lett. **13**, 2317 (2013).
[11] H. R. Vutukuri, Ph.D. thesis, Utrecht University, 2012.
[12] Y. Ma, W. Li, E. C. Cho, Z. Li, T. Yu, J. Zeng, Z. Xie, and Y. Xia, ACS Nano **4**, 6725 (2010).
[13] L. Rossi, S. Sacanna, W. T. M. Irvine, P. M. Chaikin, D. J. Pine, and A. P. Philipse, Soft Matter **7**, 4139 (2011).
[14] S. C. Glotzer and M. J. Solomon, Nat. Mater. **6**, 557 (2007).
[15] J. Henzie, M. Grünwald, A. Widmer-Cooper, P. L. Geissler, and P. Yang, Nat. Mater. **11**, 131 (2012).
[16] Y. Bai, T. Yang, Q. Gu, G. Cheng, and R. Zheng, Powder Technol. **227**, 35 (2012).
[17] J. Zhang, Z. Luo, B. Martens, Z. Quan, A. Kumbhar, N. Porter, Y. Wang, D.-M. Smilgies, and J. Fang, J. Am. Chem. Soc. **134**, 14 043 (2012).
[18] M. Eguchi, D. Mitsui, H.-L. Wu, R. Sato, and T. Teranishi, Langmuir **28**, 9021 (2012).
[19] Z. Quan, W. S. Loc, C. Lin, Z. Luo, K. Yang, Y. Wang, H. Wang, Z. Wang, and J. Fang, Nano Lett. **12**, 4409 (2012).
[20] J. J. Choi, K. Bian, W. J. Baumgardner, D.-M. Smilgies, and T. Hanrath, Nano Lett. **12**, 4791 (2012).
[21] Y. Zhang, F. Lu, D. van der Lelie, and O. Gang, Phys. Rev. Lett. **107**, 135701 (2011).
[22] L. Rossi, S. Sacanna, W. T. M. Irvine, P. M. Chaikin, D. J. Pine, and A. P. Philipse, Soft Matter **7**, 4139 (2011).
[23] S. Torquato and Y. Jiao, Nature (London) **460**, 876 (2009).
[24] J. de Graaf, R. van Roij, and M. Dijkstra, Phys. Rev. Lett. **107**, 155501 (2011).
[25] U. Betke and M. Henk, Comput. Geom. **16**, 157 (2000).
[26] C. B. Murray, C. R. Kagan, and M. G. Bawendi, Annu. Rev. Mater. Sci. **30**, 545 (2000).
[27] H. Minkowski, Nachr. K. Ges. Wiss. Göttingen **11**, 311 (1904).
[28] J. Burnet, *Greek Philosophy, Part 1: Thales to Plato* (Macmillan, London, 1914), 1st ed.
[29] J. V. Field, Arch. Hist. Exact Sci. **50**, 241 (1997).
[30] R. D. Batten, F. H. Stillinger, and S. Torquato, Phys. Rev. E **81**, 061105 (2010).
[31] R. Ni, A. P. Gantapara, J. de Graaf, R. van Roij, and M. Dijkstra, Soft Matter **8**, 8826 (2012).
[32] P. F. Damasceno, M. Engel, and S. C. Glotzer, ACS Nano **6**, 609 (2012).
[33] U. Agarwal and F. A. Escobedo, Nat. Mater. **10**, 230 (2011).
[34] P. F. Damasceno, M. Engel, and S. C. Glotzer, Science **337**, 453 (2012).
[35] G. van Anders, N. K. Ahmed, R. Smith, M. Engel, and S. C. Glotzer, arXiv:1304.7545.
[36] F. Smallenburg, L. Filion, M. Marechal, and M. Dijkstra, Proc. Natl. Acad. Sci. U.S.A. **109**, 17 886 (2012).
[37] M. Marechal, U. Zimmermann, and H. Löwen, J. Chem. Phys. **136**, 144506 (2012).
[38] See Supplemental Material at http://link.aps.org/supplemental/10.1103/PhysRevLett.111.015501 for more details regarding the simulation methods, free-energy calculations, and crystal structures.
[39] L. Filion, M. Marechal, B. van Oorschot, D. Pelt, F. Smallenburg, and M. Dijkstra, Phys. Rev. Lett. **103**, 188302 (2009).
[40] A. Haji-Akbari, M. Engel, A. S. Keys, X. Zheng, R. G. Petschek, P. Palffy-Muhoray, and S. C. Glotzer, Nature (London) **462**, 773 (2009).
[41] E. R. Chen, M. Engel, and S. C. Glotzer, Discrete Comput. Geom. **44**, 253 (2010).
[42] J. de Graaf, L. Filion, M. Marechal, R. Roij, and M. Dijkstra, J. Chem. Phys. **137**, 214101 (2012).
[43] D. Eberly, Intersection of Convex Objects: The Method of Separating Axes, http://www.geometrictools.com/.
[44] Y. Kallus and V. Elser, Phys. Rev. E **83**, 036703 (2011).
[45] U. Agarwal and F. A. Escobedo, J. Chem. Phys. **137**, 024905 (2012).